CERN LINAC4 CHOPPER DUMP: OPERATIONAL EXPERIENCE AND FUTURE UPGRADES

C. J. Sharp[*], R. Franqueira Ximenes[†], M. Calviani[‡], D. Grenier, C. Y. Mucher, E Grenier-Boley,
C. Torregrosa, J. R. Hunt, L. S. Esposito, G. Costa, P. Andreu Muñoz, A. M. Krainer,
European Organization for Nuclear Research (CERN), CH-1211 Geneva, Switzerland

Abstract

The Chopper Dump in the Linac4 accelerator at CERN is a beam-intercepting device responsible for the absorption of the 3 MeV H⁻ ion beam produced by the Linac4 source and deflected upstream by an electromagnetic chopper. It allows a portion of the beam, which would otherwise fall into the unstable region of the radiofrequency buckets in the Proton Synchrotron Booster, to be dumped at low energy with minimal induced radiation. It may also be used to absorb the entire beam. With peak currents of 25 to 45 mA and shallow penetration, this results in large deposited energy densities, thermal gradients and mechanical stresses. Additional constraints arise from geometric integration, vacuum and radiation protection requirements. Material selection, beam-matter interaction studies and thermo-structural analyses are important aspects of the design process. The Chopper Dump underwent modification in 2019 following observed material degradation in the original version of the device. The experience gained, modifications made and observations noted since then are detailed herein. Against this background, the design and analysis of an upgraded device, intended to cope with future operational conditions, is outlined and discussed.

INTRODUCTION

Chopping of the 3 MeV H⁻ beam in CERN's Linac4 accelerator allows bunches that would fall into the unstable region of the radiofrequency buckets of the PS booster to be dumped at low energy [1]. A chopping system consisting of electrostatic plates and quadrupole magnets is used to deflect particles vertically onto a conical dump in the medium energy beam transport (MEBT) line. Chopping at low energy minimises the required chopping element strength and induced radiation, but results in more demanding low-penetration conditions for the absorbing surface. The dump must absorb the entire beam when required and dissipate the resulting heat so as not to exceed material limits on temperature or stress. Additional challenges in the design arise from tight geometric constraints, vacuum and radiation protection.

Material degradation in a previous version of the dump prompted installation of a modified version during 2019 [2]. This has operated successfully at 25 mA peak dumped current but is predicted not to withstand future conditions up to 45 mA. Activation due to ^{65}Zn production also restricts long term use. A project to consolidate the dump is ongoing.

---

* calum.james.sharp@cern.ch
† rui.franqueira.ximenes@cern.ch
‡ marco.calviani@cern.ch

OPERATIONAL EXPERIENCE

Nickel-Coated Device

The original dump, first operated in 2013, consisted of a GlidCop® AL-60 core (Fig. 1a) – a dispersion-strengthened copper-based metal-matrix composite desired for its high thermal conductivity and good mechanical properties – with the internal surface coated in nickel to reduce activation [3].

Observed Degradation

In 2019, material degradation in the form of delamination and local melting of the nickel was observed (Fig. 1b), a concern for device integrity and potential introduction of debris in the beamline. Subsequent analysis concluded that the degradation was a result of a loss of local heat conduction due to subsurface cracks or voids in the coating, potentially caused by plastic deformation and low-cycle fatigue during the pulse-cooldown cycle [2]. Hydrogen implantation and blistering was identified as another possible cause.

Figure 1: (a) GlidCop® core, (b) damaged Ni coating [2].

Modifications

A modified version of the dump with the nickel coating removed (except for a small region at the aperture) was installed in August of that year. With the beam impinging directly on the GlidCop® substrate, this provides better heat conduction and increased resilience owing to the material's superior thermo-mechanical properties. Device activation is increased but acceptable in the short term.

Operation and Subsequent Inspection

The modified device has operated during Linac4 commissioning and the start of Run 3 during 2019-2022. An inspection in the 2021 year-end technical stop observed no sign of melting or delamination problems as experienced in the previous device. Some minor changes were noted, however are not thought to have a significant impact on continued operation in 2022. These included discolouration (darkening) approximately in the region of beam impact (Fig. 2) thought to be caused by migration of intrinsic carbon to the

surface of the copper. This phenomenon, particularly under annealing temperatures and in the presence of hydrogen (of which the beam is a source), is detailed by studies on the chemical vapour deposition of graphene [4, 5].

Reflective surface marks could indicate some minor deterioration of ridges left behind after machining. However, no worsening of damage to the remaining nickel at the aperture of the dump was observed. Finally, it was noted that the beam impact position appears further downstream than the nominal case, potentially putting at risk downstream equipment and supporting the inclusion of a more comprehensive alignment system in future.
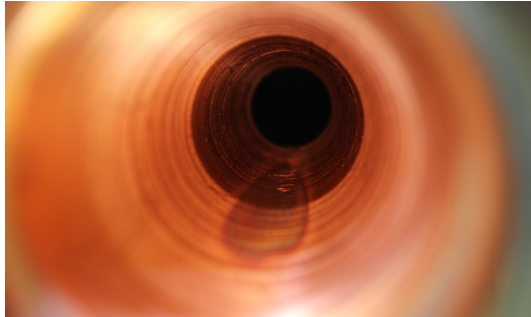

Figure 2: 2021 inspection – GlidCop® surface.

UPGRADE

Whilst operating successfully at 25 mA dumped current, finite element studies indicate the dump cannot withstand higher intensities planned for the future [6]. Radiological constraints on production of ^{65}Zn from direct exposure of copper to the beam also prohibit its use in the long term.

The upgrade currently underway is specified to withstand peak dumped currents of 27 mA (Run 3) and 45 mA (Run 4) with dumping of the entire 800 μs pulse at 0.83 Hz. This results, respectively, in 81 kW and 135 kW pulse power, and 54 W and 90 W average power (an 80% increase on the existing 25 mA specification which yields 75 kW pulse power and 50 W average power). The exclusion of highly conductive copper as a material option makes managing the concentrated energy deposition an even greater challenge.

Conceptual Design

The initial idea was to create a device similar to the existing one, but using Inconel® 625 (a nickel superalloy) as the core material. However, whilst this offered advantageous properties, mechanically and radiologically (as isotopes produced in nickel are short-lived) [7], its low thermal conductivity resulted in unacceptably high temperatures.

This prompted a more comprehensive redesign (Fig. 3) with R4550® isostatically-formed graphite [8], which is used extensively in beam-intercepting devices [9, 10]. However, its porosity means it cannot serve as the vacuum chamber nor host water-cooling channels. Hence, a shrink-fitted stainless steel jacket with a helical cooling channel was introduced with a precise interference to ensure good thermal contact.

A 3-point adjustable support platform and fiducial markers were included to facilitate full control of the alignment.
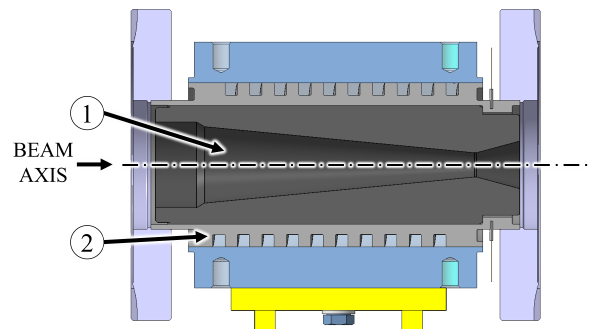
Figure 3: CAD model vertical cross section – graphite core (1) with cooling jacket (2).

Beam-Matter Interaction Studies

The Fluka Monte-Carlo simulation code [11, 12] was used to simulate the beam-material interaction. This provided a distribution of deposited energy density throughout the material, highlighting the shallow penetration of around 20 μm into the conical surface and high deposited energy densities up to 34.2 kJ/cm^3 per pulse in the 45 mA case.

Finite Element Studies

Thermal (steady-state and transient) and structural (steady-state and quasi-static) finite element analysis (FEA) was completed in ANSYS® Workbench 2020 R2 [13].

A two-scale modelling approach consisted of a coarse global model (Fig. 4) of the core and cooling jacket plus a finer sub-model of the beam-intercepting surface.
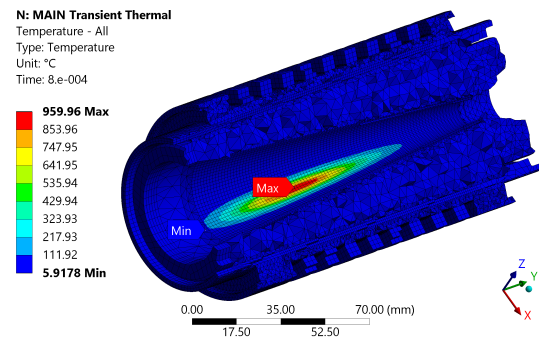

Figure 4: Global model – temperature plot (end of pulse).

Meshing created a global model with 432 000 elements and a sub-model with 78 000 elements with sizing controls used to match the array of energy deposition data. Element aspect ratio was unavoidably high; however, with small deformations and well-formed elements, this was deemed acceptable and confirmed by basic mesh convergence studies.

Thermal boundary conditions in the global model consisted of a convection condition applied on the water-cooling channel with 25 °C fluid temperature and a heat transfer coefficient of 7000 W/m^{2}K, plus the beam loading applied as a 2D surface heat flux (flattened from the 3D energy deposition array). Then, in the sub-model, temperatures from the global model were transferred to the cut boundary surfaces, and the beam loading was applied with a higher-fidelity three-dimensional distribution of heat generation.

Structurally, the shrink-fitting pre-stress was accounted for by including the real interference in the global model geometry and resolving the contact to a specified penetration tolerance at the beginning of the simulation. A fixed support boundary condition was applied on the downstream jacket edge which will be welded to the downstream flange. In the sub-model, cut-boundary displacements were transferred from the global model. In both cases, the temperature results from thermal simulations were applied to simulate the thermal stress.

The sub-model results (Table 1) indicated, in the 45 mA case, a peak temperature of 1054 °C. Although high, this remains below the limits imposed by the onset of sublimation.

Table 1: Selected Thermo-Structural FEA Results – Full Dumping of 800 µs Pulse

Result	27 mA	45 mA
Steady state max. temperature [°C]	35.2	42.2
Transient peak temperature [°C]	629.8	1054.2
Minimum principal stress [MPa]	(-)46.9	(-)75.7

Stresses in the core are generally compressive owing to the shrink-fitting stress. In the region of maximum stress, bi-axial compression dominates. The failure criterion is therefore considered simply as when the minimum principal stress exceeds the compressive strength. For bi-axial compression, this is consistent with the Mohr-Coulomb criterion implemented in ANSYS®. Comparing the worst case minimum principal stress with an ultimate compressive strength of 130 MPa yields an acceptable factor of safety of 1.7.

The calculation to specify the shrink-fitting interference between the core and cooling jacket was carried out analytically in the first case, using the Lamé equations for thick cylinders, and later with finite element simulations. Manufacturing limitations required that calculations be made at the limits of the tolerances so as to ensure sufficient interface pressure and acceptable stresses in all cases. The diametric interference specified was 30-70 µm.

Fatigue

A phenomenological S-n curve assessment of fatigue due to the 0.83 Hz pulse-cooldown cycle highlighted slim safety margins, although uncertainties were large owing to a lack of material data. A second calculation considered that the cyclic stresses are extremely superficial, and that even if a crack were to exist on the inner core surface penetrating to a depth of 0.3 mm (where the stress is effectively non-cyclic), the crack tip stress intensity factor would likely not exceed the fracture toughness and the crack would not propagate.

Cooling System Performance

Cooling system calculations were performed with analytical equations using the empirical Dittus-Boelter correlation for calculation of the Nusselt number and thus the heat transfer coefficient. With the 6 mm square channel specified, this yielded an estimated heat transfer coefficient of 7000 W/m²K which was then applied in the FEA studies.

Preliminary CFD analysis broadly confirmed the analytical findings, although velocities near the inner wall may be reduced by centrifugal effects. However, the system is not considered particularly sensitive to this as critical temperatures are dominated by local conduction on a short timescale.

Microstructural Effects

Whilst temperatures in the homogeneous FEA were well below sublimation point, there is some concern that isolated grains in the microstructure of graphite with reduced capacity for conduction could reach higher temperatures.

An analytical micro-model of an isolated 10 µm grain of graphite with the peak deposited energy density applied and radiation to the surrounding bulk material modelled by the Stefan-Boltzmann law indicated temperatures may indeed reach sublimation point.

In a parallel approach, integrating the specific heat capacity over temperature up to 3800 K yields an energy requirement of 7050 kJ/kg. Filtering the energy deposition map by this threshold gives a region (accounting for up to 45% or 48 J of energy deposition) in which isolated grains may adiabatically reach this temperature. If a sublimation energy requirement of 41 900 kJ/kg is now considered (adding latent heat to the previous figure), and assuming that 1% of the material consists of isolated grains, then the sublimation rate is estimated as 1.14×10^{-8} kg per pulse.

If sustained, this equates to 0.034 g per hour, which would be unacceptable. However, as isolated grains sublimate, the vulnerable portion of material is expected to deplete, meaning sublimation may cease after an initial "bake-out" period. Re-condensation and deposition may also occur.

Experimental tests in a 45 keV test stand are planned to assess this potential for surface degradation under low energy beam conditions.

Device Production

Trials have been carried out to verify the assembly process and associated precision manufacturing requirements. Shrink-fitting requires that the core and jacket be heated to 250 °C such that different degrees of thermal expansion generate a clearance to allow insertion of the core. Metrology analysis of the interface surfaces will ensure compliance with tolerances and reduce uncertainty over the interface pressure, thermal contact and stresses in the core.

The graphite will also undergo vacuum firing treatment to reduce outgassing at high operational temperatures, followed by residual gas analysis to assess vacuum compliance.

CONCLUSIONS

Building on past operational experience, a new design for CERN's Linac4 Chopper Dump has been proposed and analysed. Whilst further studies on the integrity of graphite under shallow beam penetration are ongoing, the device is foreseen to be installed in 2022/23.

REFERENCES

[1] A. Lombardi, "Commissioning of the Low-Energy Part of Linac4," CERN, Geneva, Switzerland, Tech. Rep. CERN-ACC-2014-394, 2014, https://cds.cern.ch/record/2062590

[2] C. Torregrosa Martin, A. Ciccotelli, and L. S. Esposito, "Thermo-mechanical analysis and reconditioning of the linac4 chopper internal dump," CERN, Technical Note EDMS:2384553, 2021.

[3] L. Arnaudon *et al.*, "Linac4 Technical Design Report," CERN, Geneva, Switzerland, Tech. Rep. CERN-AB-2006-084, CARE-Note-2006-022-HIPPI, 2006, revised version submitted on 2006-12-14 09:00:40, https://cds.cern.ch/record/1004186

[4] M. H. Khaksaran and I. I. Kaya, "On the dynamics of intrinsic carbon in copper during the annealing phase of chemical vapor deposition growth of graphene," *ACS Omega*, vol. 4, no. 6, pp. 9629–9635, 2019, doi:10.1021/acsomega.9b00681

[5] Y. Çelik, W. Escoffier, Y. Ming, E. Flahaut, and E. Suvacı, "Relationship between heating atmosphere and copper foil impurities during graphene growth via low pressure chemical vapor deposition," *Carbon*, vol. 109, pp. 529–541, 2016, doi:10.1016/j.carbon.2016.08.057

[6] M. Widorski, C. Torregrosa Martin, M. Calviani, and J. Lallement, "Linac4 medium energy beam transport line dump," CERN, Functional Specification EDMS:2435672, 2021.

[7] L. Bruno, M. Magistris, and M. Silari, "Conceptual design and radiological issues of a dump for the 3 MeV test facility," CERN, Geneva, Switzerland, Tech. Rep. CERN-SC-2004-008-RP-TN, 2004.

[8] *Sigrafine® r4550*, TDS R4550.00, SGL Carbon, 2019, https://www.sglcarbon.com/pdf/SGL-Datasheet-SIGRAFINE-R4550-EN.pdf

[9] I. Leitão and C. Maglioni, "Design specifications for the linac4 main and lbe dump cores," CERN, Engineering Specification EDMS:1256894, 2014.

[10] C. Maglioni, "The linac4 commissioning dump," CERN, Engineering Specification EDMS:1182648, 2013.

[11] C. Ahdida *et al.*, "New capabilities of the fluka multi-purpose code," *Frontiers in Physics*, vol. 9, no. 788253, 2022, doi:10.3389/fphy.2021.788253

[12] G. Battistoni *et al.*, "Overview of the fluka code," *Annals of Nuclear Energy*, vol. 82, pp. 10–18, 2015, doi:10.1016/j.anucene.2014.11.007

[13] Ansys®, *Ansys mechanical enterprise*, version 2020 R2.